Computation of STM Images of Carbon Nanotubes

P. LAMBIN,[1] G. I. MÁRK,[2] V. MEUNIER,[3] L. P. BIRÓ[2]

[1]*Laboratoire de physique du solide, FUNDP, 61 Rue de Bruxelles, B5000 Namur, Belgium*
[2]*Research Institute for Technical Physics and Materials Science, Budapest, Hungary*
[3]*Computer Science and Mathematics Division, Oak Ridge National Laboratory, Oak Ridge, Tennessee*

Received 23 February 2003; accepted 24 February 2003

DOI 10.1002/qua.10587

ABSTRACT: Scanning tunneling microscopy (STM) is the only probing technique that allows for the investigation of both the topography and the electronic structure of carbon nanosystems at a subnanometer resolution. The interpretation of the STM images of carbon nanostructures involves complications that are normally absent in the study of planar crystalline surfaces. The complications typically appear from a number of quantum effects responsible for distortions in the microscope image of a nano-object. Because of these difficulties, computer simulation plays an extremely important role in the analysis of experimental data. In the current article, we report on two theoretical approaches developed for aiding in the interpretation and understanding of the formation of the STM image of a nanotube: first, the quantum mechanical dynamics of a wave packet, which allows for the modeling of the flow of the tunneling current between a tip and a nanotube supported by a substrate; and, second, a tight-binding perturbation theory that allows for the explicit calculation of realistic STM images and scanning tunneling spectra of carbon nanostructures. An atlas of computed STM images is provided for a series of 27 single-wall nanotubes with diameter around 1.3 nm.

Key words: carbon nanotubes; nanostructures; perturbation theory; scanning tunneling microscopy; wave packet

Correspondence to: P. Lambin; e-mail: philippe.lambin@fundp.ac.be

Contract grant sponsor: Belgian Office for Scientific, Technical, and Cultural Affairs. Contract grant number: P5/01.

Contract grant sponsor: OTKA. Contract grant number: T 043685.

Contract grant sponsor: Belgian FNRS.

Contract grant sponsor: Hungarian Academy of Sciences.

Contract grant sponsor: U.S. Department of Energy. Contract grant number: DE-AC05-00OR22725.

International Journal of Quantum Chemistry, Vol 95, 493–503 (2003)

Introduction

The discovery of the fullerene [1] opened new avenues for the science of carbon nanostructures. In addition to the fullerenes, a large variety of carbon nanosystems are known: nanotubes [2], onions [3], helices [4], disks and cones [5], rings [6] and tori [7], nanohorns [8], tripods [9], and Y-branched tubes [10]. Apart from being very interesting from a theoretical point of view, carbon nanostructures have a wide range of potential applications, owing to their remarkable physical and chemical properties.

Exploring the applications of carbon nanostructures in a reliable way requires a sample characterization as precise as possible. To that end, very few techniques to characterize an isolated nanostructure at the atomic scale are available. Among them, only scanning tunneling microscopy in the topographic (STM) and spectroscopic (STS) modes offer the possibility to study both the atomic and electronic structures of the same nanostructure with a subnanometer resolution. However, this property makes the interpretation of STM images a challenging task, because the influences of the topography and the electronic structure have to be identified and separated. Several other factors, the STM tip geometry being the most significant, also affect the imaging mechanism. For all these reasons, the simulation of STM images turns out to be a useful tool for a correct interpretation of STM experimental data.

The already vast literature devoted to the characterization of carbon nanotubes by STM and STS techniques has been reviewed in two recent articles [11, 12]. With a blunt tip, no atomic resolution can be achieved on a nanotube and the STM provides only a geometric information [13]. Furthermore, tip-shape convolution effect makes the width D of a cross-sectional profile along a nanotube appear typically much larger than the actual tube diameter. More precisely, D is related to the apparent height h of the tube by the approximate relation $D = \sqrt{8Rh}$, where R is the curvature radius of the tip, as shown in Ref. [14].

Atomic resolution can be achieved when the STM tip presents a nanoprotrusion effectively terminated with a single atom. Even with this ideal tip, only the topmost part of a nanotube can be imaged. The first STM images revealing partial atomic corrugation on a carbon nanotube were published by Ge and Sattler [15], who performed experiments on multiwall nanotubes. The interpretation of the images was made difficult because of the interactions between the concentric layers: the interlayer coupling is indeed a probable cause for the formation of superstructures observed in the images, usually attributed to a Moiré pattern. The first atomic-resolution topographic STM images and STS spectra on single-wall nanotubes were reported simultaneously and independently by two groups [16, 17]. In both experiments, the samples were synthesized by the laser ablation technique and imaged at low temperature on a gold substrate. Still, carbon atoms could not be resolved individually. In the topographic images, corrugation holes appear at positions corresponding to the centers of the hexagons of the honeycomb structure, defining a triangular lattice with parameter 0.246 nm. These corrugation dips are surrounded by protruding features at the location of the C—C bonds. All C—C bonds of a nanotube are not revealed in the same manner; that effect often destroys the honeycomb symmetry in the STM images [18]. Tight-binding [19, 20] and ab initio [21] calculations of the STM image confirm this observation.

The two wrapping indices of an isolated single-wall nanotube can be deduced in principle from the STM image by measuring the diameter and the chiral angle. Unfortunately, this ultimate characterization is not easy. In principle, the chiral angle of the nanotube can be determined from a measurement of the angle between the tube axis and the centers of the closest row of hexagons. However, the STM image is often distorted by the curvature of the lattice [19, 22], which entails a systematic error in the measurement of the angles. Deriving the diameter from STM information is also challenging, mostly because of the tip-shape convolution effect mentioned above. To circumvent this effect, the diameter is conveniently obtained by fitting the STM current measured at various locations above the nanotube and its support with exponential laws [23]. Yet, it is difficult to account for the variation of the tunneling barrier when the STM tip crosses a nanotube. Today, the most reliable and conventional way to evaluate the diameter consists in measuring the positions of the van Hove singularities in the electronic density of states via standard STS measurements and comparing them with their known relationship with the nanotube radius [24, 25].

To sum up the discussion, quantum mechanical effects in tunneling microscopy are specific to the nanotube geometry and must be unmistakably understood for a correct interpretation of the STM images of carbon nanotubes. In the current article, two theoretical approaches are considered for understanding the unique features of the STM image of a nanotube. First, quantum mechanical dynamics of a wave packet (WP) is used to investigate how the tunneling current sets up between the tip, the nanotube, and its support. Second, a tight-binding perturbation theory allows for the calculation of realistic STM images of carbon nanotubes. A series of computed images is provided for 27 nanotubes, with diameters ranging from 1.17 to 1.39 nm. It is hoped that this atlas of images will be helpful in the identification of single-wall nanotubes from their STM topographical data.

Wave-Packet Dynamics

To be imaged with an STM, a carbon nanotube has to be deposited on a support with atomically flat, and conducting, surface. Highly oriented pyrolitic graphite (HOPG) and Au (111) terraces are the most frequently used supports. As opposed to the tunneling into a bulk sample, the electrons have to cross two tunnel barriers: one between the STM tip and the nanotube, another one between the nanotube and its support. To address the problem of STM tunneling within its full geometric complexity, we used a simple jellium potential to represent the STM tip, the carbon nanotube, and the support [26]. The same potential background (-9.81 eV) was used for the tip, support, and tube. Within the jellium approximation, all carbon nanotubes are metallic. Nevertheless, this approximation captures the essential physics of the tunneling phenomena. In our calculations, the STM tip is modeled by a hyperboloid of 0.5 nm apex radius, protruding out of a flat medium. The carbon nanotube is represented by a cylinder of 1 nm diameter and 0.14 nm thickness, floating above the planar support at a distance of 0.335 nm. The tip/nanotube tunnel gap is 0.4 nm.

The current density is determined by calculating the scattering of a WP incident onto the potential barriers between the tip, nanotube, and support. The initial WP is constructed from the stationary states of the free-electron electrode from which the WP arrives, either the tip holder or the support bulk. For the calculations illustrated here, a spherically symmetric Gaussian WP was used with initial wave vectors $\vec{k}$ corresponding to a 5-eV average translational kinetic energy with a distribution of about 1 eV. The total tunnel current at a given STM bias is calculated as a statistical average of the partial currents obtained with WPs of different allowed incident energies and wave vectors and weighted according to the band structure of the two electron reservoirs.

The tunneling probability for a given initial WP is determined from the time-dependent wavefunction $\psi(\vec{r}, t)$ computed from the time-dependent Schroedinger equation by the split-operator Fourier transform method [27]. In this method, the time-evolution operator $\exp(-iH\Delta t/\hbar)$ is approximated by the symmetrical unitary product

$$\exp(-iH\Delta t/\hbar) = \exp(-iK\Delta t/2\hbar)\exp(-iV\Delta t/\hbar)\exp(-iK\Delta t/2\hbar) \tag{1}$$

where Δt is the evolution time step. The error associated with that approximation is $o(\Delta t^3)$. The effect of the kinetic energy propagator $\exp(-iK\Delta t/2\hbar)$ on $\psi(\vec{r}, t)$ is a simple multiplication by the factor $\exp(-i\hbar \mathrm{k}^2\Delta \mathrm{t}/4\mathrm{m})$ of the $\vec{k}$-representation of the wavefunction, $\phi(\vec{k}, t)$ obtained by fast Fourier transform (FFT) of $\psi(\vec{r}, t)$. The effect of the potential energy propagator is a simple multiplication in the $\vec{r}$ representation obtained by inverse FFT.

The constant-current STM topographic profile through a carbon nanotube was first calculated in two dimensions [26], showing that as long as the electronic structure of the nanotube and that of the support may be considered similar, the major image distortions arise from pure geometric tip-shape convolution already discussed above. The STS spectra were also computed by the same technique. The calculations revealed asymmetric I–V curves of pure geometric origin [28]. The asymmetry is amplified when a contact between the tip and nanotube or nanotube and support is established, as the result of a mechanical deformation of the nanotube exerted by the STM tip.

The usefulness of the WP dynamics method is completely revealed when using it in three-dimensional simulations [29]. The computer simulation clearly shows that during tunneling, the charge spreads along the nanotube. Figure 1 illustrates the time evolution of the density probability $|\psi(\vec{r}, t)|^2$ in the STM nanotube substrate model. The nanotube has a length of 15 nm in these calculations. At time $t = 0$, the WP is launched from the STM tip electrode. After 1.8 fs, electrons begin to tunnel into the nanotube and flow around its circumference. Most

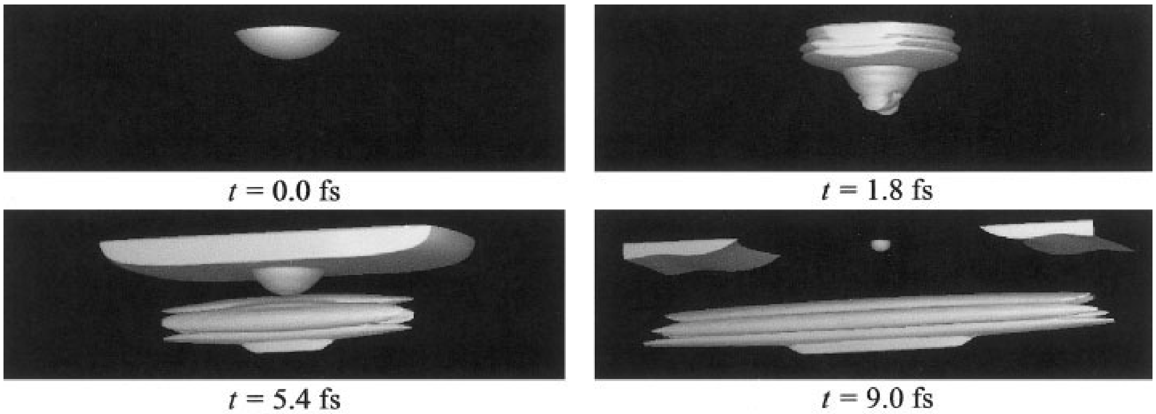

$t = 0.0$ fs

$t = 1.8$ fs

$t = 5.4$ fs

$t = 9.0$ fs

FIGURE 1. Dynamics of the probability density of a WP coming from the tip bulk and tunneling through the model tunnel junction; $|\psi(\vec{r}, t)|^2$ is visualized by the time evolution of a constant density surface. The horizontal size of the presentation window is 15.36 nm.

of them are reflected back into the upper electrode, leading to a disk-shaped interference pattern in the figure. At $t = 5.4$ fs, the WP tunnels into the support surface while spreading along the tube. Simultaneously, the WP propagates in the upper electrode on both sides along the horizontal direction. After 9 fs, the probability at the tip apex region is already smaller than that on the nanotube. The structuration of the constant density surface around the nanotube is due to predominant excitations of bound eigenstates of the cylindrical well with $m = 2$ and $m = 3$ angular momentum numbers. The first m states of a jellium tube fall within a small energy window around 5 eV. These states are excited because of the scattering of the WP when it enters the tube.

Tight-Binding Theory

As shown in the previous section, electron tunneling into a supported nanotube is a complex problem because of the presence of two barriers. Figure 1 clearly indicates that the dynamics of the WP proceeds in two quasisequential processes. In the first process, when the electrons tunnel from the tip into the nanotube, the support plays little role. In the second process, the STM tip itself plays little role. One could reasonably well reproduce the first process by ignoring the support and by assuming that the nanotube is in contact with two electrodes at both ends, through which the spreading charges can be evacuated into the external STM circuit. Compared with the floating nanotube, this electrical setup certainly affects the absolute value of the transmission coefficient of the STM problem, but it has little influence on the imaging process itself. Ab initio calculations of the STM image of a nanotube on Au using the Tersoff–Hamann formalism show that this is actually the case [21].

From this point on, the support is ignored and the STM current is directly derived from the nanotube. By treating the coupling interaction v between the STM tip and the isolated nanotube in first-order perturbation theory, the tunnel current between them writes

$$I = \frac{2\pi e}{\hbar} \int_{-\infty}^{+\infty} dE [f_t(E) - f_s(E)] \times \sum_{\alpha,\beta} |\langle \alpha | v | \beta \rangle|^2 \delta(E - E_\alpha) \delta(E - E_\beta) \quad (2)$$

where α and β are electronic states of the unperturbed tip (t) and sample (s), respectively, with Fermi occupation probabilities $f_t(E)$ and $f_s(E)$. In tight binding, assuming one orbital per atom for the sake of simplicity, the electronic states of the tip and sample are linear combinations of atomic orbitals located on the corresponding sites i and j:

$$|\alpha\rangle = \sum_{i \in t} \chi_i^\alpha |\eta_i\rangle, \quad |\beta\rangle = \sum_{j \in s} \psi_j^\beta |\theta_j\rangle. \quad (3)$$

The insertion of these linear combination of atomic orbitals (LCAO) expressions in Eq. (2) yields the following expression for the current at 0 K [30]

$$I = (2\pi)^2 \frac{e}{h} \int_{E_F^s - eV}^{E_F^s} dE \sum_{i,i' \in t} \sum_{j,j' \in s} \upsilon_{ij} \upsilon^*_{i'j'} \times n^t_{ii'}(E^t_F - E^s_F + eV + E) n^s_{jj'}(E) \quad (4)$$

where the E_Fs are the Fermi levels of the unperturbed systems, and $\upsilon_{ij} = \langle \chi_i | \upsilon | \theta_j \rangle$ is the tip-sample coupling element. The energy levels of the tip sites have been shifted to accommodate the bias and contact potential of the junction. In Eq. (4),

$$n^s_{jj'}(E) = (-1/\pi) \mathrm{Im}\, G^s_{jj'}(E + i0^+) \quad (5)$$

with $G^s_{jj'}(z)$ a Green function element of the sample for the complex energy z. A similar expression is defined on the tip side. The diagonal elements $n^t_{ii}(E)$ and $n^s_{jj}(E)$ are the local densities of states on sites i and j of the tip and sample, respectively. These elements are computed by recursion [31]. This technique, originally designed for the calculation of diagonal elements of the Green function, also gives access to nondiagonal elements [32]. For a real symmetric Hamiltonian matrix with one orbital per atom, nondiagonal elements can be obtained as follows

$$G_{jj'}(z) = G_{j'j}(z) = \left\langle \frac{\theta_j + \theta_{j'}}{\sqrt{2}} \middle| (z - H)^{-1} \middle| \frac{\theta_j + \theta_{j'}}{\sqrt{2}} \right\rangle - \frac{1}{2} [G_{jj}(z) + G_{j'j'}(z)]. \quad (6)$$

The nanotube Green function was computed with C π orbitals only, assuming a constant hopping interaction of −2.9 eV between first-neighbor atoms.

For the applications illustrated below, the STM current was calculated with Eq. (4) by considering a single atom i at the tip apex with an s atomic orbital, like in Tersoff–Hamann theory [33]. A Gaussian function of 6 eV full width at half maximum was chosen to represent the density of states of the tip at the apex $n^t_{ii}(E)$. The tip-sample coupling interactions are sp Slater–Koster hopping terms having the following expression [19]:

$$\upsilon_{ij} = \upsilon_0 w_{ij} e^{-d_{ij}/\lambda} \cos \theta_{ij} \quad (7)$$

$$w_{ij} = e^{-a d^2_{ij}} \Big/ \sum_{j'} e^{-a d^2_{ij'}} \quad (8)$$

where d_{ij} is the distance between the tip atom i and the sample atom j, θ_{ij} is the angle between the orientation of the π orbital on site j and the ij direction (see Fig. 2). The Gaussian weight factor w_{ij} was introduced for convergence reasons. The parameters used are $\lambda = 0.085$ nm and $a = 60$ nm^{-2}. The prefactor υ_0 does not influence the imaging process as long as absolute values of the current are not required.

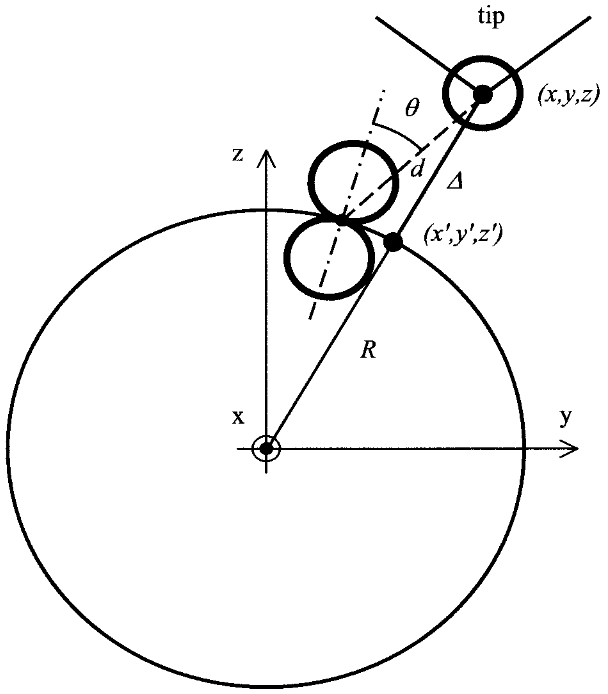

FIGURE 2. The STM tip with an s orbital at the apex and the nanotube with a π orbital on each carbon atom (just one is drawn for clarity). The largest tip–nanotube coupling element is taking place along the normal Δ to the nanotube.

Constant-current images of single-wall nanotubes were computed using the tight-binding formalism sketched above. The reference value of the current is chosen as the one computed when the tip is located 0.5 nm above an atom along the normal direction to the tube. When the tip moves away from this position, its z-coordinate is updated, to keep the current constant. For a given position of the tip apex, it is clear from Eq. (8) that the largest interaction υ_{ij} is realized when the atom is located closest to the radial direction of the tip, because the tip–atom distance is the shortest there and cos θ is close to one (see Fig. 2). In other words, the current flows predominantly along the normal direction to the tube rather than along the vertical direction, as it would from a flat sample. Wave-packet dynamics calculations for a tip placed aside the nanotube

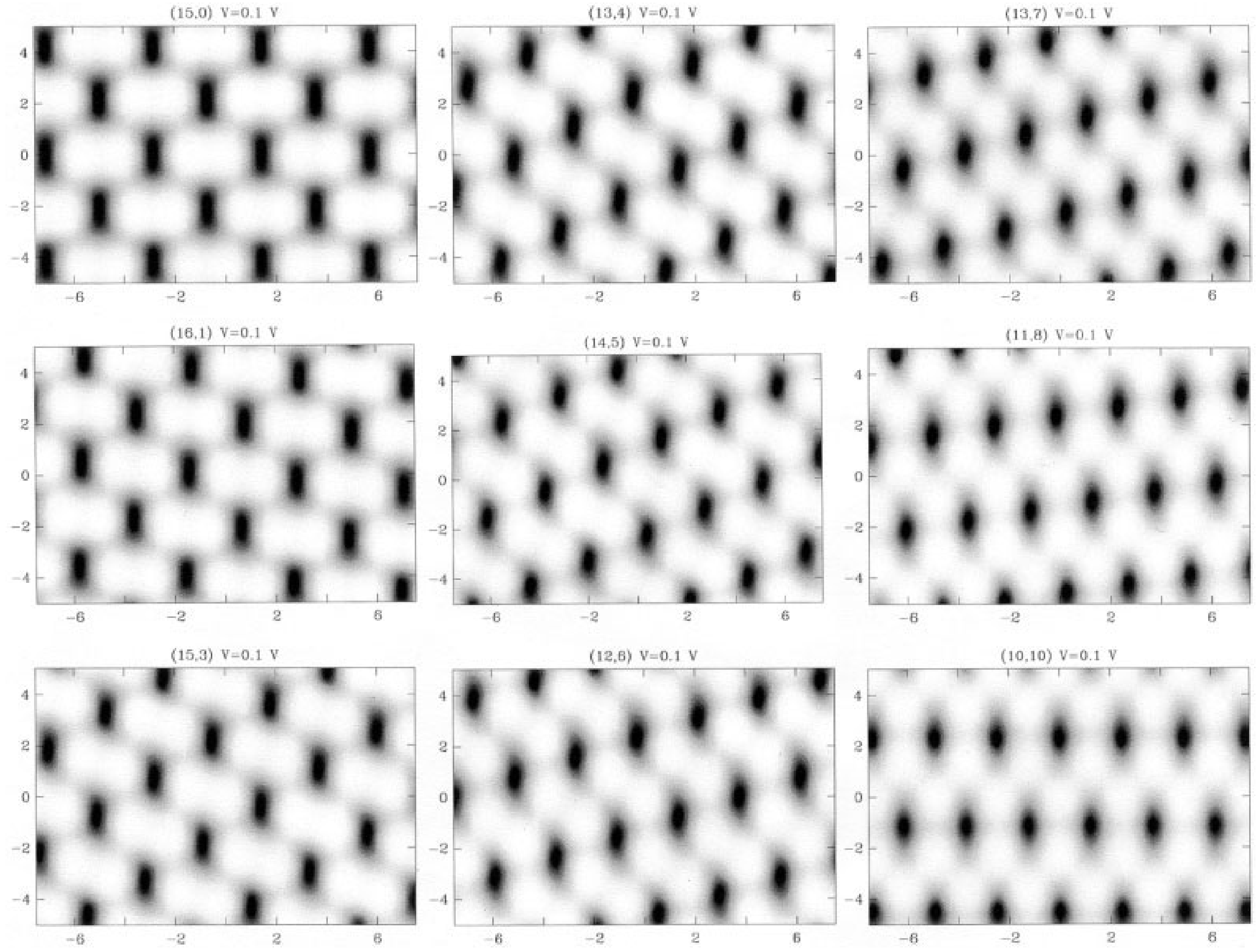

FIGURE 3. The STM images of nine metallic single-wall nanotubes computed with a tip potential $V = +0.1$ V. The gray scale represents the axial distance $\rho = \sqrt{y^2 + z^2}$ of the tip apex at constant current versus its x (horizontal) and y (vertical) coordinates (see Fig. 2). Near the median line $y = 0$, ρ is close to the vertical coordinate z of the tip as measured experimentally. All coordinates are expressed in Å.

beautifully confirm this effect [26]. When the current is assumed to flow radially, a C atom at coordinates (x', y', z') on the tube is imaged when the tip has horizontal coordinates $x = x'$ and $y = y'(R + \Delta)/R$, as shown in Figure 2. Here the x-axis is parallel to the tube axis (i.e., perpendicular to the drawing), y is measured normally to the axis, R is the tube radius, and Δ is the tip–nanotube distance. The imaged atomic structure of the nanotube is therefore stretched by the factor $(R + \Delta)/R$ in the y direction [19]. Because of this distortion, the angles between the three zigzag chains of C atoms measured in an STM image are larger than 30°. The distortion is conveniently corrected by squeezing the y-axis in such a way as to restore the correct angles [25].

In the computed images displayed here, the coordinates x and y are measured along the horizontal and vertical directions, respectively. As discussed above, the images are distorted along the vertical direction. STM images of 27 single-wall nanotubes (with diameters ranging from 1.17 to 1.39 nm) were computed, among which nine nanotubes are metallic and 18 are semiconducting. For an (n, m) nanotube, the metallic or semiconducting character depends on whether $n - m$ is a multiple of three or not [34, 35].

For a metallic nanotube, the calculations indicate that the tip potential has little influence on the STM image as long as it does not exceed a few tenths of volts. The computed image does not depend on the potential sign either. Figure 3 illustrates how the

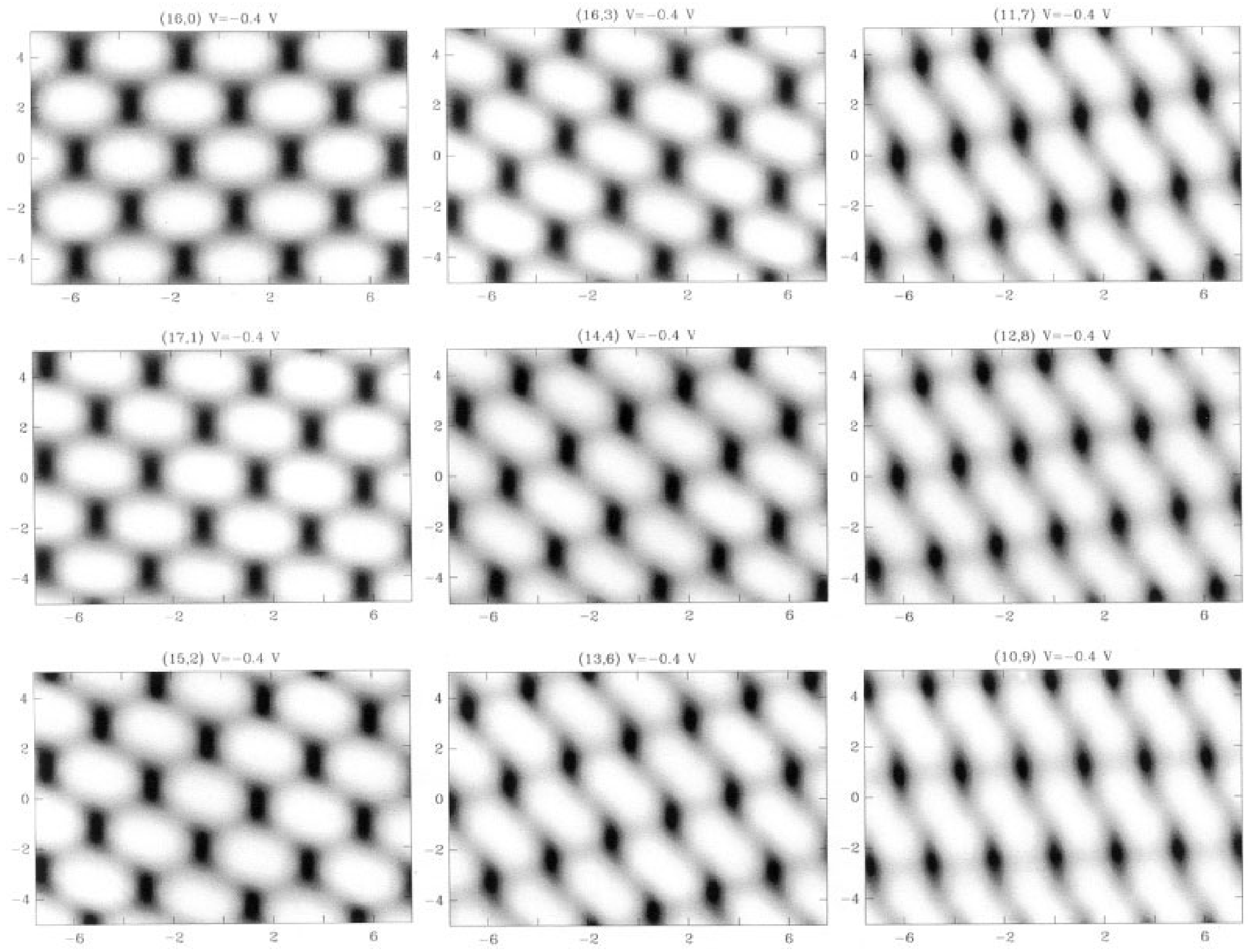

FIGURE 4. The STM images of nine semiconductor (n, m) nanotubes with $n - m = M(3) + 1$ computed with a tip potential $V = -0.4$ V.

STM images of metallic nanotubes depend on the chiral angle. For instance, the image of the (15,0) zigzag nanotube displays a strong anisotropy in the C—C bonds: the ones parallel to the axis form elongated horizontal protrusions. By opposition, there is a local minimum of corrugation at the center of the bonds inclined at 60° from the axis. As the chiral angle of the nanotube increases, the strongest bonds progressively rotate, whereas, simultaneously, the bond anisotropy progressively washes out. For the armchair (10,10) nanotube, all the bonds look the same and the honeycomb structure of the graphitic network is clearly recognizable, apart from the stretching of the image along the y coordinate discussed above.

The images of a semiconducting nanotube depend on the polarity of the bias potential. If we neglect any contact potential that would shift the Fermi level of the semiconductor, the tip potential must exceed half the band gap of the nanotube to produce a tunneling current. The values $+0.4$ and -0.4 V were selected for the calculations. When the tip is negative, the unoccupied states of the nanotube are probed. Inversely, a positive tip explores the occupied states. Interestingly, the image of a semiconducting (n, m) nanotube depends not only on the sign of the bias potential but also on whether $n - m$ is a multiple of three plus one or minus one [20].

Figures 4 and 5 show the images of nine semiconductors with $n - m = M(3) + 1$ computed for a negative and a positive bias, respectively [$M(3)$ denotes any integer multiple of 3]. There is again a strong anisotropy of the bonds in the case of a zigzag nanotube here (16,0). For a negative tip (Fig. 4), the bonds parallel to the axis of the (16,0) nano-

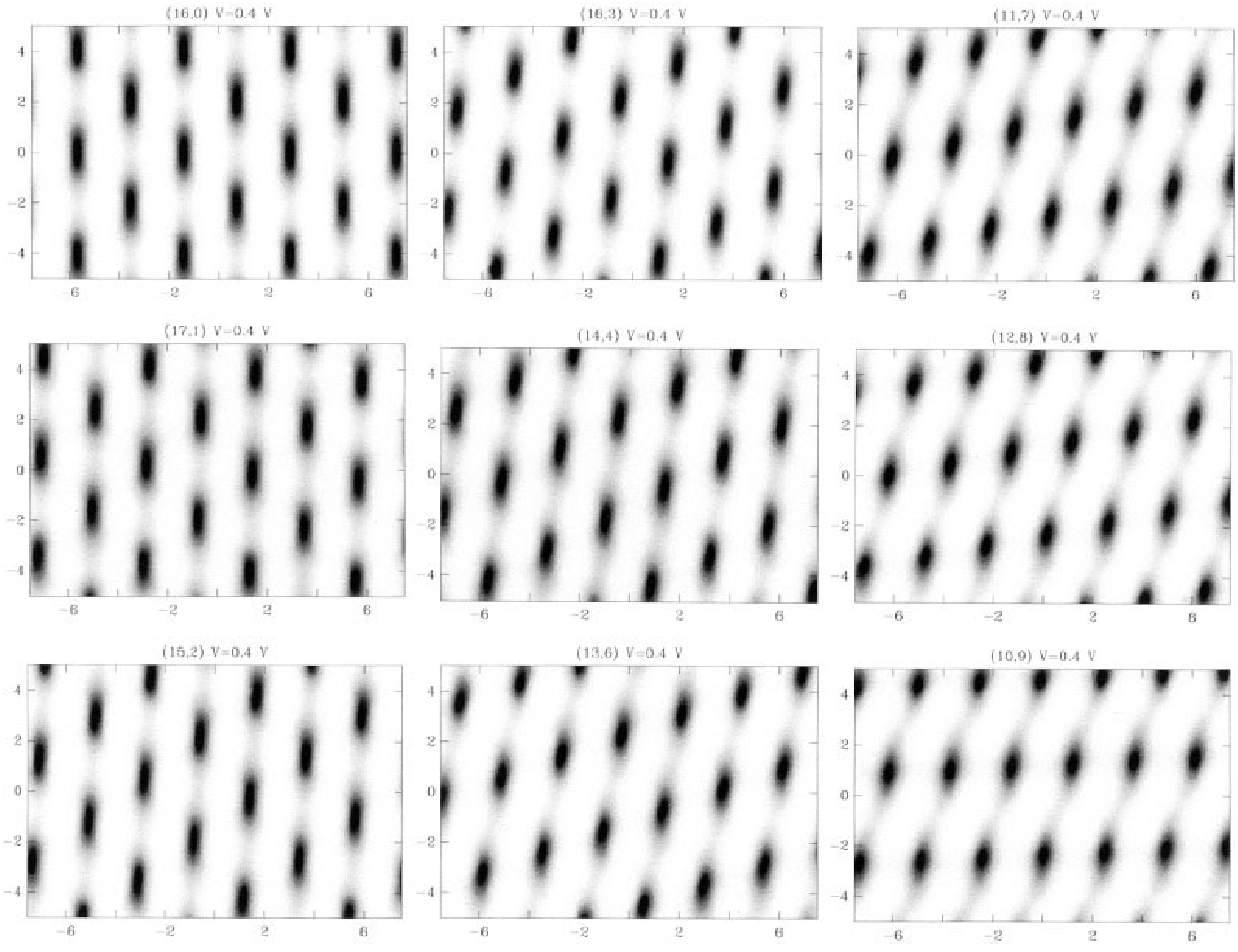

FIGURE 5. Same as in Figure 4 for a tip potential $V = +0.4$ V.

tube are highlighted and form isolated protrusions in the image. An increase of the chiral angle of the nanotube produces a rotation of the strongest bonds, which progressively join together and form stripes that spiral around the nanotube. With the nanotube chiralities considered here, these spiral stripes are all right-handed (the images of the enantiomer nanotubes are mirrored images). With a positive tip (Fig. 5), the handedness of the spiral stripes is reversed. This remarkable complementarity of the STM images upon reversing the bias was observed experimentally [36]. For the zigzag (16,0) nanotube imaged with a positive tip, the strongest bonds are the ones that zigzag around the tube, in remarkable contrast to the image computed with a negative tip.

The asymmetry of the STM image of a semiconducting nanotube upon reversing the bias potential arises from the nondiagonal elements of the Green function. In particular, the elements $n_{jj'}(E)$ between two first-neighbor sites are important because they govern the appearance of the C—C bonds in the STM image. For the (16,0) nanotube, $n_{jj'}$ for the bonds parallel to the axis is large and positive near the bottom of the conduction band [37], which indicates a bonding character [38]. As stated by Eq. (4), a positive $n_{jj'}$ element adds a positive contribution to the STM current when the tip is above a parallel jj' bond. Still near the lowest unoccupied molecular orbital (LUMO) state, $n_{jj'}$ is negative for the bonds at 60° from the axis. These bonds have an antibonding character, and the current above them is therefore reduced. Altogether, these results explain why the parallel bonds protrude more than the inclined ones in the STM image of (16,0) when $V = -0.4$ V (Fig. 4). At the top of the valence band, the sign of the $n_{jj'}$ elements is inverted, because they are odd functions of $E - E_F$, and the contrast of the

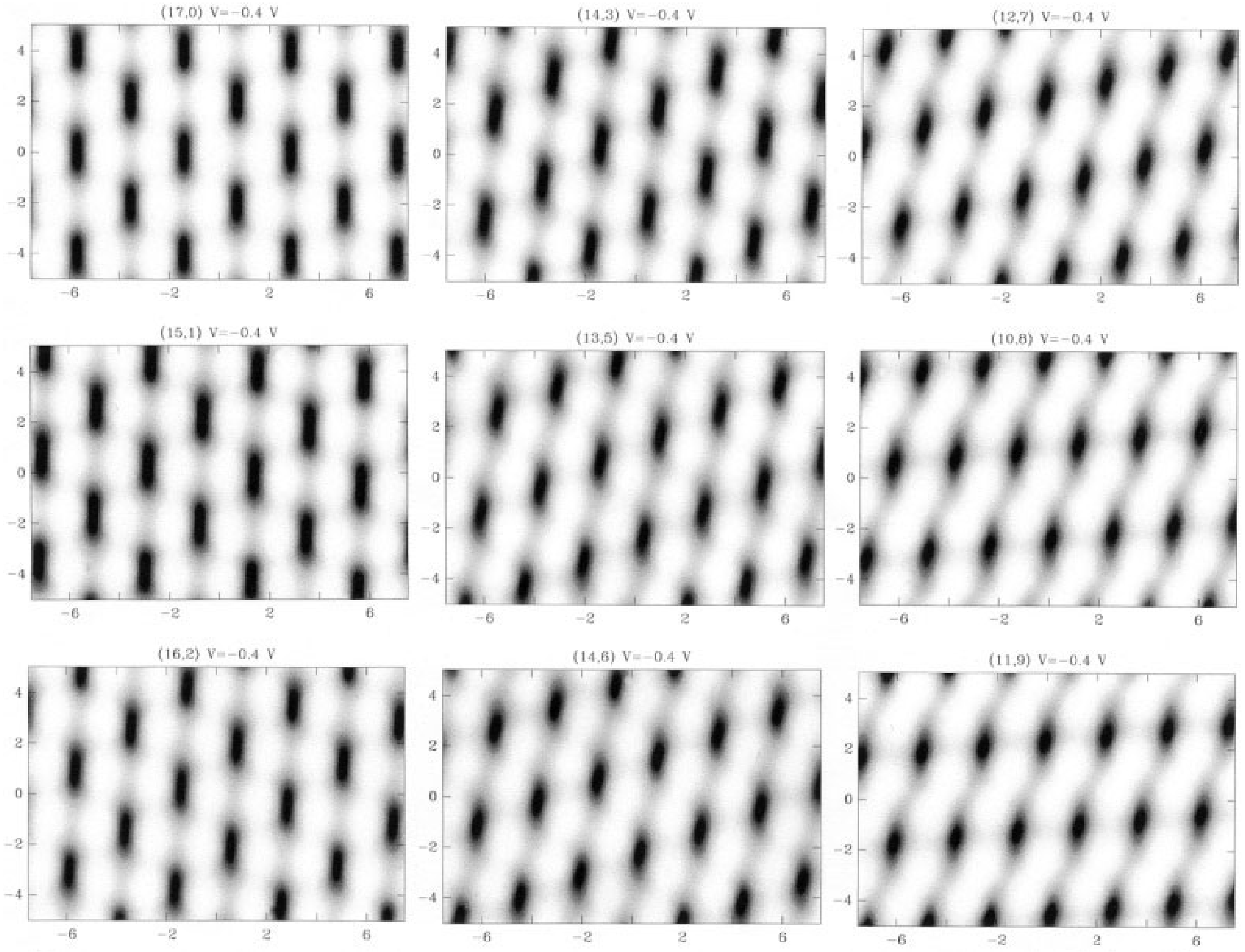

FIGURE 6. The STM images of nine semiconductor (n, m) nanotubes with $n - m = M(3) - 1$ computed with a tip potential $V = -0.4$ V.

corresponding bonds changes in the STM image when the bias potential is reversed.

The computed STM images of nine semiconducting nanotubes with $n - m = M(3) - 1$ are shown in Figures 6 and 7 for negative and positive tip potentials, respectively. The images look like the ones computed for the previous family of semiconducting nanotubes for reversed bias potential. For instance, the nanotube (17,0) imaged with $V = -0.4$ V looks like the image of (16,0) computed with $V = +0.4$ V. As shown in Ref. [37], this complementarity of the STM images arises from the fact that the first-neighbor elements $n_{jj'}(E)$ of (17,0) are very close to the ones of (16,0) computed for an energy E symmetric with respect to the Fermi level. In other words, the LUMO and highest occupied molecular orbital states exchange their first-neighbor $n_{jj'}$ densities of states.

Conclusions

The electronic process of the STM imaging of a supported nanostructure relies on complex quantum mechanical effects. Part of the complexity comes from the peculiar geometry of the tunneling barriers. A WP originating at the tip has to tunnel through two barriers, and the dynamics of these two tunneling processes are different, as illustrated in Figure 1. Even when the problem is simplified to a point where the support is ignored, complex phenomena still take place. It follows that the STM image of an isolated nanotube is not a straightforward representation of its atomic structure. The STM images computed with a π-based tight-binding Hamiltonian demonstrate that the honeycomb symmetry of the graphitic network is almost always

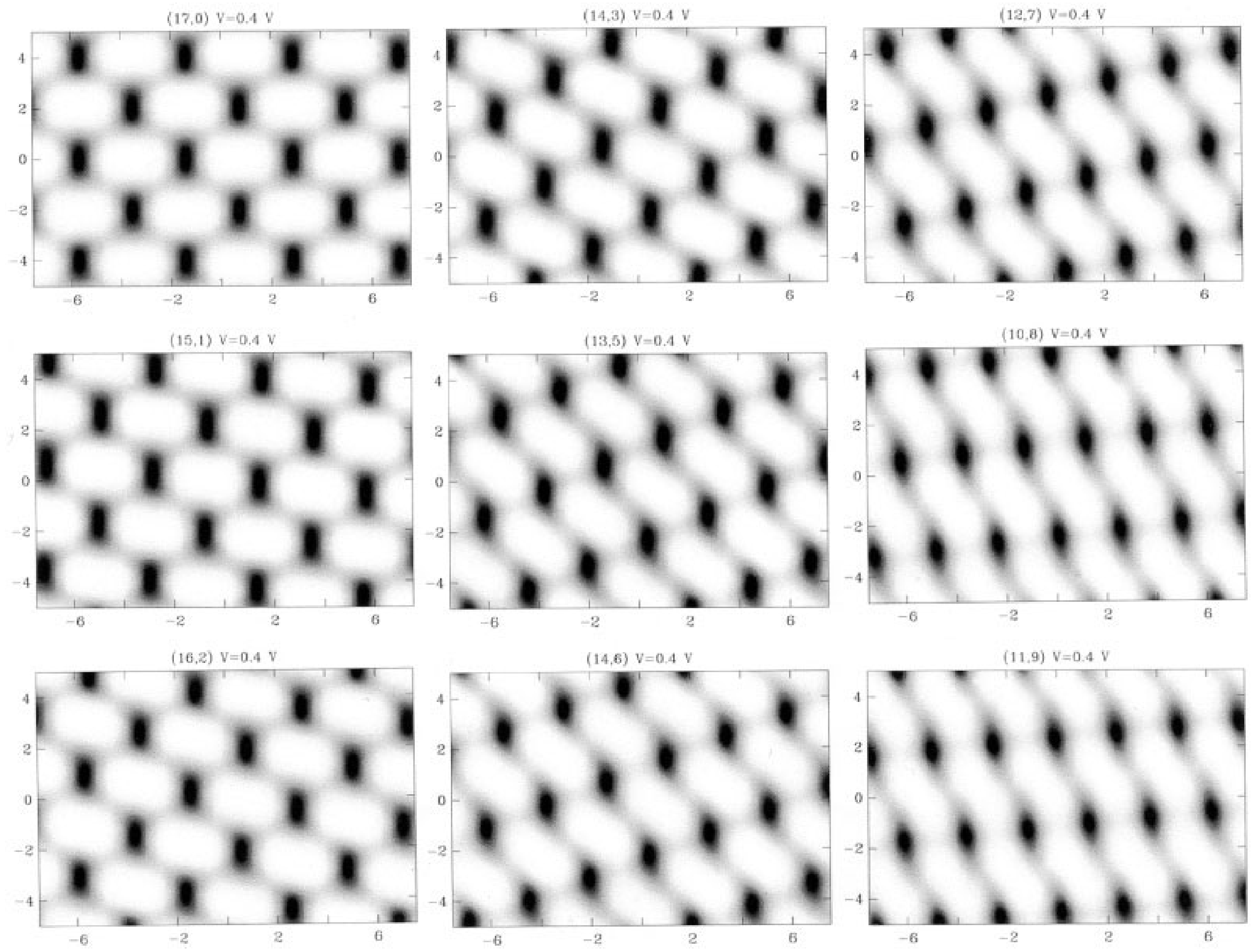

FIGURE 7. Same as in Figure 6 for a tip potential $V = +0.4$ V.

broken by electronic effects. It should be noted that the STM images of armchair nanotubes are the only ones to exhibit the full symmetry of its structure. Even in this case the symmetry is broken by electron back-scattering caused by local defects [36]. Images of semiconducting nanotubes have a systematic broken symmetry, with complementary contrast changes upon reversing the STM tip potential.

ACKNOWLEDGMENTS

This work was partly funded by the IUAP research project P5/01 on "Quantum Size Effects in Nanostructured Materials" of the Belgian Office for Scientific, Technical, and Cultural Affairs. The work in Hungary was supported by OTKA grant T 043685. This work also benefited from financial support from the Belgian FNRS and the Hungarian Academy of Sciences and was sponsored in part by the Mathematical, Information and Computational Sciences Division, Office of Advanced Scientific Computing Research of the U.S. Department of Energy under contract no. DE-AC05-00OR22725 with UT-Battelle, LLC. The 3D WP calculations were done on the Supercomputing Facility of the Hungarian NIIF.

References

1. Kroto, H. W.; Heath, J. R.; O'Brien, S. C.; Curl, R. F.; Smalley, R. E. Nature 1985, 318, 162.
2. Iijima, S. Nature 1991, 354, 56.
3. Ugarte, D. Nature 1992, 359, 707.
4. Amelinckx, S.; Zhang, X. B.; Bernaerts, D.; Zhang, X. F.; Ivanov, V.; Nagy, J. B. Science 1994, 265, 635.

5. Krishnan, A.; Dujardin, E.; Treacy, M. M. J.; Hugdahl, J.; Lynum, S.; Ebbesen, T. W. Nature 1997, 388, 451.
6. Liu, J.; Dai, H.; Hafner, J. H.; Colbert, D. T.; Smalley, R. E.; Tans, S. J.; Dekker, C. Nature 1997, 385, 780.
7. Sano, M.; Kamino, A.; Okamura, J.; Shinkai, S. Science 2001, 293, 1299.
8. Iijima, S.; Yudasaka, M.; Yamada, R.; Bandow, S.; Suenaga, K.; Kokai, F.; Takahashi, K. Chem Phys Lett 1999, 309, 165.
9. Le Normand, F.; Constant, L.; Ehret, G.; Speisser, C. J Mater Res 1999, 14, 560.
10. Li, J.; Papadopoulos, C.; Xu, J. Nature 1999, 402, 253.
11. Odom, T. M.; Huang, J. L.; Lieber, C. M. J Phys Condens Matter 2002, 14, R145.
12. Biró, L. P.; Lambin, P. In Nalwa, H. S., Ed. Encyclopedia of Nanoscience and Nanotechnology; American Scientific Publishers: Fairfield, NJ, 2003.
13. Gallagher, M. J.; Chen, D.; Jacobsen, B. P.; Sarid, D.; Lamb, L. D.; Tinker, F. A.; Jiao, J.; Huffman, D. R.; Seraphin, S.; Zhou, D. Surf Sci 1993, 281, L335.
14. Biró, L. P.; Lazarescu, S.; Lambin, P.; Thiry, P. A.; Fonseca, A.; Nagy, J. B.; Lucas, A. A. Phys Rev B 1997, 56, 12490.
15. Ge, M.; Sattler, K. Science 1993, 260, 515.
16. Wildoer, J. W. G.; Venema, L. C.; Rinzler, A. G.; Smalley, R. E.; Dekker, C. Nature 1998, 391, 59.
17. Odom, T. W.; Huang, J. L.; Kim, P.; Lieber, C. M. Nature 1998, 391, 62.
18. Venema, L. C.; Wildoer, J. W. G.; Dekker, C.; Rinzler, A. G.; Smalley, R. E. Appl Phys A 1998, 66, S153.
19. Meunier, V.; Lambin, P. Phys Rev Lett 1998, 81, 5888.
20. Kane, C. L.; Mele, E. J. Phys Rev B 1999, 59, R12759.
21. Rubio, A.; Sanchez-Portal, D.; Artacho, E.; Ordejon, P.; Soler, J. M. Phys Rev Lett 1999, 82, 3520.
22. Kleiner, A.; Eggert, S. Phys Rev B 2001, 64, 113402.
23. Odom, T. W.; Huang, J. L.; Kim, P.; Ouyang, M.; Lieber, C. M. J Mater Res 1998, 13, 2380.
24. Kim, P.; Odom, T.; Huang, J. L.; Lieber, C. M. Phys Rev Lett 1999, 82, 1225.
25. Venema, L. C.; Meunier, V.; Lambin, P.; Dekker, C. Phys Rev B 2000, 61, 2991.
26. Márk, G. I.; Biró, L. P.; Gyulai, J. Phys Rev B 1998, 58, 12645.
27. Feit, M. D.; Fleck, J. A. Jr. J Chem Phys 1983, 78, 301.
28. Márk, G. I.; Biró, L. P.; Gyulai, J.; Thiry, P. A.; Lucas, A. A.; Lambin, P. Phys Rev B 2000, 62, 2797.
29. Márk, G. I.; Koós, A.; Osváth, Z.; Biró, L. P.; Benito, A. M.; Maser, W. K.; Thiry, P. A.; Lambin, P. Diamond Related Mater 2002, 11, 961.
30. Kobayashi, K.; Tsukada, M. J Vac Sci Technol A 1990, 8, 170.
31. Haydock, R.; Heine, V.; Kelly, M. J. J Phys C Solid St Phys 1975, 8, 2591.
32. Inoue, J.; Okada, A.; Ohta, Y. J Phys Condens Matter 1995, 5, L465.
33. Tersoff, J.; Hamann, D. R. Phys Rev Lett 1983, 50, 1998.
34. Hamada, N.; Sawada, S. I.; Oshiyama, A. Phys Rev Lett 1992, 68, 1579.
35. Mintmire, J. W.; Dunlap, B. I.; White, C. T. Phys Rev Lett 1992, 68, 631.
36. Clauss, W.; Bergeron, D. J.; Freitag, M.; Kane, C. L.; Mele, E. J.; Johnson, A. T. Europhys Lett 1999, 47, 601.
37. Lambin, P.; Meunier, V. In Biró, L. P.; Bernardo, C. A.; Tibbetts, G. G.; Lambin, P., Eds. Carbon Filaments and Nanotubes: Common Origins, Differing Applications? NATO Science Series E, Vol. 372; Kluwer Academic Publishers: Dordrect, 2001, pp. 233–244.
38. Meunier, V.; Senet, P.; Lambin, P. Phys Rev B 1999, 60, 7792.